Origin of ferroelectricity and superconductivity with nontrivial electronic topology in fluorinated Nb_2N

Xin-Zhu Yin (尹新竹),[1] Na Jiao (焦娜),[1,*] Jinlian Lu (卢金炼),[3] Meng-Meng Zheng (郑萌萌),[1] Hong-Yan Lu (路洪艳),[1,†] and Ping Zhang (张平)[1,2]

[1]*School of Physics and Physical Engineering, Qufu Normal University, Qufu 273165, China*
[2]*Institute of Applied Physics and Computational Mathematics, Beijing 100088, China*
[3]*Department of Physics, Yancheng Institute of Technology, Yancheng, Jiangsu 224051, China*

(Received 30 April 2024; revised 23 August 2024; accepted 29 August 2024; published 13 September 2024)

Two-dimensional (2D) intrinsic superconductors with nontrivial topological band and vertical ferroelectricity exhibit fascinating characteristics for achieving electrostatic control of quantum phases. Only a few such 2D materials have been theoretically predicted. In this paper, based on first-principles calculations, we explore the superconductivity and ferroelectric properties in fluorinated 2D Nb_2N. In the stable Nb_2NF_2, H_3-Nb_2NF_2 breaks the spatial inversion symmetry, exhibiting vertical ferroelectric. More interestingly, it not only possesses intrinsic superconductivity with superconducting transition temperatures (T_c) of 10 K, but also exhibits nontrivial band topology. H_1-Nb_2NF_2 shows topological band and superconductivity with T_c of 32 K, surpassing most of the 2D conventional topological superconductors' candidates. Our research has enriched 2D superconducting materials with nontrivial band topology and ferroelectric properties, and provided a theoretical basis for the preparation of devices switching between superconducting and ferroelectric states with external electric field.

DOI: 10.1103/PhysRevB.110.094507

I. INTRODUCTION

Ferroelectric materials have great technological importance for realizing nonvolatile random-access memory. Two-dimensional (2D) ferroelectric materials have a rich application field, including but not limited to 2D ferroelectric-based energy harvesters [1], tunnel junctions [2], field-effect transistors [3], photodetectors [4], and photocatalytic elements [5]. 2D ferroelectric metals not only possess a spontaneous and switchable electric polarization through the application of an external electronic field but also exhibit metallic property. Recently, the advantages of 2D ferroelectric metal have been experimentally confirmed and theoretically predicted in 2D layered and van der Waals materials [6,7]. Experimentally, the 2D topological semimetal WTe_2 was confirmed to exhibit spontaneous out-of-plane electric polarization, which can be switched using gate electrodes [8]. Several 2D materials that can sustain ferroelectric metal states have been theoretically predicted, such as monolayer CrN [9], two-unit-cell thick $LiOsO_3$ thin film [10], 1T'-WTe_2 multilayer [11,12], etc. Thus, 2D ferroelectric metal offers compelling advantages in tunable electronic behavior via conventional electrostatic techniques to exploit ferroelectricity to control other electronic states.

Superconductivity tunable with ferroelectricity can be used to make a superconducting switch driven by external electric field [7,13]. Recent investigations have experimentally revealed that bilayer T_d-$MoTe_2$ simultaneously exhibits ferroelectric switching and superconductivity [7]. Layered transition-metal carbides, nitrides, and carbon-nitrides named MXenes are an emerging family of 2D materials. The potential superconductivity of MXenes was theoretically assessed by the Eliashberg formalism [14]. Since the synthesis of $Ti_3C_2T_x$, the progress in the synthesis and development of MXenes crystals with and without the required functional groups have become more mature [15–18], which also promotes the intensity of research on these materials. Surface functionalization can modulate the superconductivity of 2D MXenes [19–21]. The fluorinated 2D Nb_2N has been reported to have good reversible out-of-plane electrical polarization and metallic properties in the H_3 phase [22]. Thus, MXenes have the potential application in low-power-consumption ferroelectric-based superconductor electronic devices.

The coexistence of superconductivity and nontrivial band topology is highly desired for exploring exotic quantum physics [23–25]. Achieving electrostatic control of the superconductivity quantum phase and band topology is at the frontier of condensed matter research. So far, few 2D ferroelectric superconductivity materials with nontrivial band topology have been predicted or discovered except for ferroelectric-superconductivity heterobilayers, such as $IrTe_2/In_2Se_3$ [25]. Theoretically, ferroelectric-superconductivity heterobilayer was predicted to be a useful scheme to achieve the ferroelectric tunable superconductivity and band topological [25]. The preparation process of heterojunctions is constrained by lattice matching and other issues, making it more attractive to search for intrinsic ferroelectric topological superconductors. This greatly inspires researchers to explore new kinds of topological superconductors regulated by ferroelectric polarization. It is expected to achieve topological superconductivity controlled by ferroelectric polarization in MXene compounds.

*Contact author: j_n2013@126.com
†Contact author: hylu@qfnu.edu.cn

 ©2024 American Physical Society

In this paper, using first-principles approaches, we systematically study the superconductivity and band topology of fluorinated Nb_2N at different adsorption sites. We demonstrate that H_3-Nb_2NF_2 not only possesses intrinsic superconductivity with T_c of 10 K, but also exhibits nontrivial band topology. H_1-Nb_2NF_2 has the highest T_c of 32 K, surpassing most of superconductors with nontrivial band topological properties. The T_c sensitively depends on the ferroelectric polarization phase. Our research is of great significance for the development of ferroelectric and superconducting coupling devices.

II. COMPUTATIONAL DETAILS

The structural and electronic properties of hydrogenated and fluorinated Nb_2N are studied based on the density functional theory calculations with the projector augmented wave (PAW) method [26,27], as implemented in the VASP package [28]. The Perdew-Burke-Ernzerhof generalized gradient approximation [29] is employed and the electron-ion interaction is described by using the PAW method. The Fermi surface (FS) is broadened by the Gaussian smearing method with a width of 0.05 eV. All the geometries are relaxed, and convergence tolerances of force and energy are set to 0.01 eV and 10^{-6} eV, respectively. A vacuum separation is set to be more than 20 Å to prevent any interactions between two neighboring monolayers. A $12\times12\times1$ Monkhorst-Pack k-point mesh is used to sample the 2D Brillouin zone (BZ). The out-of-plane electrical polarization intensity was calculated based on the macroscopic electric polarization [30]. The data processing of energy band, orbital-projected electron band structures, density of state, and orbital-projected density of state are carried out by QVASP [31] and VASPKIT [32] software packages.

To investigate the phonon dispersion and the electron-phonon coupling (EPC), the density functional perturbation theory [33] calculations are performed with the QUANTUM ESPRESSO package [34]. The kinetic energy cutoffs of 80 and 800 Ry are chosen for the wave functions and the charge densities, respectively. The Methfessel-Paxton smearing width of 0.02 Ry is used. The BZ k-point [35] grids of $48\times48\times1$ and $24\times24\times1$ are adopted for the dense and sparse self-consistent electron-density calculations, respectively. The dynamic matrix and EPC matrix elements are calculated on $12\times12\times1$ q-point meshes. The FSs colored as a function of an arbitrary scalar quantity in this paper are drawn by using the FERMISURFER program [36]. The edge states are determined through the iterative Green's function implemented in the WANNIERTOOLS package [37] and its basis set depends on the maximum localized Wannier functions [38] from the VASP2WANNIER90 interfaces [39].

The relevant calculation formulas and calculation details of superconductivity are shown in the Supplemental Material (SM) [40], which also contains Refs. [41–43].

III. RESULTS AND DISCUSSION

A. Structure and stability

In our calculations, we consider all the possible fluorine atom adsorption positions of the 1T- and 2H-Nb_2N. For Nb_2N, two niobium atoms and one nitrogen atom in the center are coordinated with octahedral geometry in the 1T phase and with trigonal geometry in the 2H phase. The 1T- and 2H-Nb_2N are crystallographically subjected to the $P\bar{3}M1$ and $P\bar{6}M2$ space groups, respectively. The stable structures after fluorination of the 1T and 2H phases are named T_1, T_2, T_3, H_1, H_2, and H_3, respectively, as shown in Fig. 1. The possible adsorption positions are consistent with the previous theoretical results [21,22], which studied the hydrogenated and fluorinated of MXene. The atom arrangement between the surface fluorine, the niobium and nitrogen atom at the top and bottom have clear differences for T_1-, T_2- and T_3-Nb_2NF_2. In the T_1 structure, these atoms are coordinated with octahedral geometry at both sides, while in the T_2 structure, these atoms are coordinated with trigonal prismatic geometry. For the T_1 phase, the F atoms vertically align with Nb atoms on the other side of the stack. As shown in Fig. 1(b), both F atoms align with the N atom to form the T_2 phase. Both T_1 and T_2 structures are crystallographically subjected to the $P\bar{3}M1$ space group. The space group of T_3-Nb_2NF_2 is $P3M1$. For T_3-Nb_2NF_2, the top side atoms are coordinated in octahedral geometry and the bottom side ones are coordinated in trigonal geometry. The lack of inversion symmetry in T_3-Nb_2NF_2 leads spontaneous electrical polarization. Finally, one F atom aligns with the Nb atom, while the other F atom aligns with the N atom to form the T_3 phase. Similarly, the three corresponding H-type configurations are referred to as H_1, H_2, and H_3 structures, as shown in Figs. 1(d)–1(f). As for the different atom arrangements between the surface fluorine, the niobium and nitrogen atom at the top and bottom sides, the fluorinated 2H-Nb_2N are named H_1-, H_2-, and H_3-Nb_2NF_2. These atoms are coordinated with trigonal geometry at both sides in the H_1 phase and with octahedral geometry at both sides in the H_2 phase. The space groups of both H_1- and H_2-Nb_2NF_2 are all $P\bar{6}M2$. For H_3-Nb_2NF_2, the top side atoms are coordinated in trigonal geometry and the bottom side ones are coordinated in octahedral geometry. The H_3-Nb_2NF_2 is crystallographically subjected to the $P3M1$ space group. The lack of inversion symmetry in H_3-Nb_2NF_2 leads to sponta-

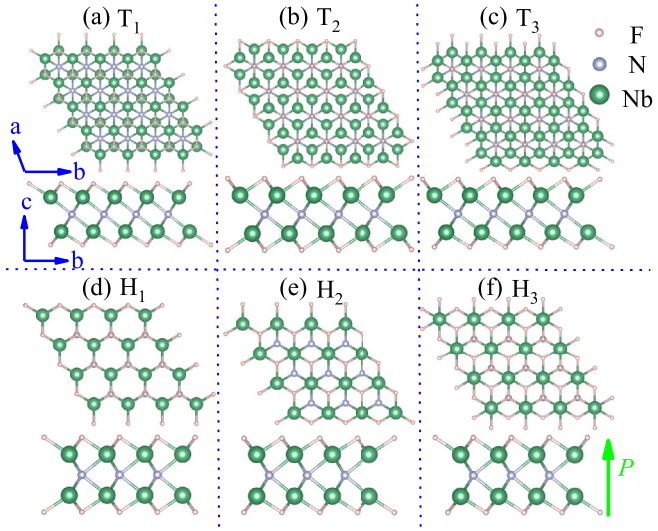

FIG. 1. Top (upper panel) and side (lower panel) views of Nb_2NF_2 in (a) T_1, (b) T_2, (c) T_3, (d) H_1, (e) H_2, and (f) H_3 phases. The direction of polarization of the material is indicated by the green arrow.

TABLE I. Calculated lattice constant a (Å), formation energy E_{form} (eV/atom), bond lengths (Å) of N-Nb and Nb-F, and the space group before and after fluorinated Nb_2N.

	a	E_{form}	$l_{\text{N-Nb}}$	$l_{\text{Nb-F}}$	Space group
$1T$-Nb_2N	3.13		2.13		$P\bar{3}M1$
$2H$-Nb_2N	2.90		2.20		$P\bar{6}M2$
T_2-Nb_2NF_2	2.97	−1.76	2.18	2.26	$P\bar{3}M1$
H_1-Nb_2NF_2	2.96	−1.77	2.21	2.25	$P\bar{6}M2$
H_3-Nb_2NF_2	2.93	−1.81	2.25	2.22 2.24	$P3M1$

neous electrical polarization. Therefore, it possesses intrinsic spontaneous ferroelectric polarization. Table I contains the lattice constants a and bond lengths of Nb-N and Nb-F for the corresponding before and after fluorinated stable structures. After fluorination, the lattice constants and the corresponding N-Nb bond lengths have a small change compared to the ones in Nb_2N. This very limited perturbation of the lattice due to F is in stark contrast with the observation of giant in-plane lattice expansion of Ti_2C with Te functionalization (over than 18%) [44]. The relaxed Nb-F bond length is about 2.2 Å in almost all cases.

To be a feasible ferroelectric and superconductor, first it should be dynamically and thermodynamically stable. For 2D materials, the requisite for a dynamic stable structure is that the phonon dispersion has no imaginary frequency. The phonon spectra of these six structures are shown in Fig. S2 (Supplemental Material) [40]. The vibration modes of the eigenvector for unstable phonons in H_2-Nb_2NF_2 are also exhibited. Through our analysis, we can find that the fluorine atoms in both vibration modes have a tendency to vibrate near that directly above the nitrogen. H_2-Nb_2NF_2 may distort into H_3-Nb_2NF_2 if fluorine atoms can cross the potential barrier and reach the top of nitrogen atom. The dynamic and thermodynamic stabilized Nb_2NF_2 are listed in Table I, and the absence of obvious imaginary frequencies in the phonon dispersion will be shown later. To explore the thermodynamical stability, the formation energy of Nb_2NF_2 is calculated by $E_{\text{form}} = [E(Nb_2NF_2) - (2E(Nb) + \frac{1}{2}E(N_2) + E(F_2))]/5$, where $E(Nb_2NF_2)$, $E(Nb)$, $E(N_2)$, and $E(F_2)$ are the energies of the Nb_2NF_2, Nb crystal (space group is $Im\bar{3}m$), nitrogen, and fluorine, respectively. The values of E_{form} for thermodynamically stabilized Nb_2NF_2 are listed in Table I and the negative value proves their thermodynamical stability.

B. Electronic structure and ferroelectric polarization properties

Figures 2(a), 2(e), and 2(i) show the orbital-projected electron band structures (PBANDs) of T_2-, H_1-, and H_3-Nb_2NF_2 along the high-symmetry line Γ-M-K-Γ, respectively. They are all metals because the Fermi energy crosses multiple bands. Figures 2(b), 2(f), and 2(j) and 2(c), 2(g), and 2(k) show the total density of states (DOS) and the DOS of the Nb, N, and F elements, and the partial DOS for T_2-, H_1-, and H_3-Nb_2NF_2, respectively. The DOS of T_2-, H_1-, and H_3-Nb_2NF_2 at the Fermi level is mainly contributed by Nb-$d_{xy} + d_{x^2-y^2}$ and Nb-$d_{xz} + d_{yz} + d_{z^2}$ orbitals, and the contributions of other elements at the Fermi level can be neglected. From the partial DOS, it can be seen that the contributions of in-plane Nb-d orbitals are larger than the out-of-plane ones to the band at the Fermi level for both H_1- and H_3-Nb_2NF_2, while the contributions of out-of-plane Nb-d orbitals for the T_2-Nb_2NF_2 is comparable with the ones of in-plane Nb-d orbitals. More interestingly, both the in-plane and out-of-plane Nb-d orbitals in H_1-Nb_2NF_2 are all larger than the ones in H_3-Nb_2NF_2 at the Fermi level because of the differences in symmetry, which may further affect the EPC. Figures 2(d), 2(h), and 2(l) are the FS of T_2-, H_1-, H_3-Nb_2NF_2, respectively. Combined with Figs. 2(a) and 2(d), we can see that there is a circular electron pocket around the Γ point of T_2-Nb_2NF_2. As shown in Fig. 2(d), there are two flower-like FSs paralleled with each other, which will be beneficial for Fermi nesting. Similarly, we can see that there are two circle FSs around the Γ point paralleled with each other in H_1-Nb_2NF_2, as shown in Fig. 2(h). For the FSs of H_3-Nb_2NF_2, the reduction of parallel FSs is mainly due to the breaking of spatial inversion symmetry along the out-of-plane direction. Thus, the H_3-Nb_2NF_2 provides another platform to study the interplay between ferroelectricity and superconductivity. In the subsequent discussion of this paper, we will only focus on the possible change in superconductivity and topological properties during the ferroelectric polarization reversal of H_3 phase.

TABLE II. The polarization parameters, including electric dipole moment p (e Å), volume V (Å^3), lattice vector c (Å), area S (Å^2), and polarization intensity P (C m^{-1}) for ferroelectric H_3-Nb_2NF_2.

	p	V	c	S	P
H_3-Nb_2NF_2	0.047	231.64	31.106	7.447	1.01×10^{-11}

Then we further demonstrate ferroelectricity in H_3-Nb_2NF_2 by investigating the in-plane averaged electrostatic potential in the out-of-plane direction, the possible kinetic pathways, and corresponding activation energy barrier of the polarization reversal between different polarized states. The out-of-plane ferroelectricity polarization intensity of 2D ferroelectricity metal equals the born effective charge per unit area, which can be calculated based on density functional perturbation theory. Table II lists the polar parameters including electric dipole moment p, volume V, lattice vector c, area S, and polarization intensity P. For H_3-Nb_2NF_2, the polarization intensity is 1.01×10^{-11} C m^{-1}, which is comparable with the value of monolayer As or Sb [45]. An external electric field can change the polarization direction of ferroelectric materials that can be reversed. Here, we use the nudged elastic band method to study the two kinetic pathways and corresponding activation energies for reversing the polarization direction of H_3-Nb_2NF_2. In the process of polarization reversal, the structure is transformed into a intermediate state, e.g., H_1 or H_2 phases, which are nonpolar, symmetric, and stable during the transformation. Figures 3(a) and 3(b) show the kinetic paths with H_1- and H_2-Nb_2NF_2 as intermediate states, respectively. It can be seen that the difference between the potential barriers of these two kinetic paths is only 0.001 eV, and the activation energy barrier of H_1 phase is lower than the one of H_2

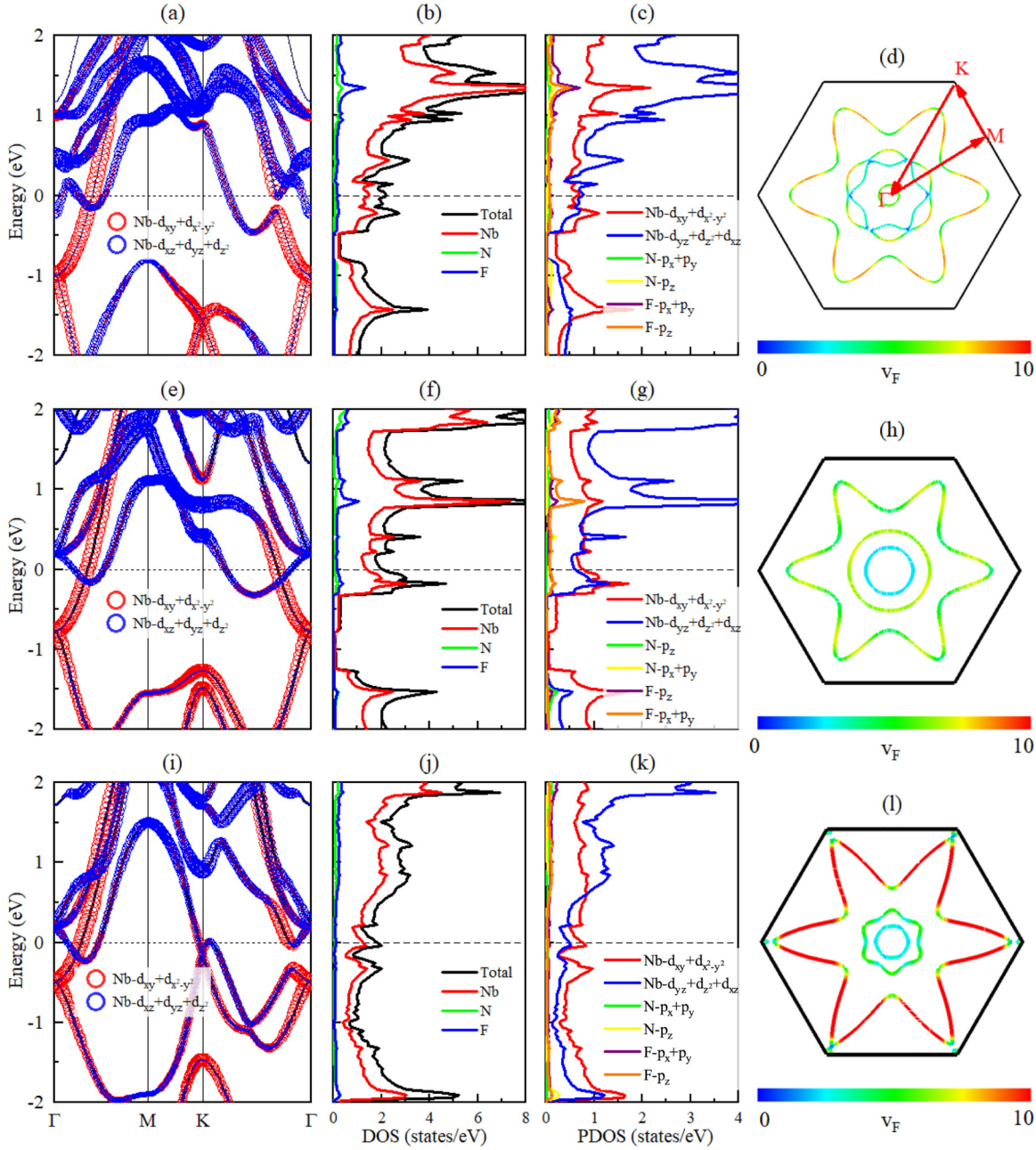

FIG. 2. (a) Orbital-projected electronic band structure of Nb along high-symmetry line Γ-*M*-*K*-Γ, (b) the total DOS and the projected DOS of Nb, N, and F, (c) the orbital-partial DOS, and (d) the FS of T_2-Nb_2NF_2. The Fermi level indicated by the dotted line is set to 0 eV, and the colors in the FS are proportional to the magnitude of the Fermi velocity v_F (10^6 ms^{-1}). (e)–(h) and (i)–(l) are similar to (a)–(d), but for H_1- and H_3-Nb_2NF_2, respectively.

intermediate states. Therefore, the probability of H_1 phase as the intermediate state of the kinetic path of H_3-Nb_2NF_2 polarization direction inversion is greater, which is consistent with the previous work by Wijethunge *et al.* [22]. Figure 3(c) illustrates the electrostatic potential of H_3-Nb_2NF_2 with respect to the out-of-plane direction and it shows that the vacuum levels at either end of the structure differ by 1.1 eV. The difference between vacuum levels and its direction (high to low) demonstrates that the ferroelectric polarization is greater than the self-depolarization field generated by the mobile carriers [22].

C. Electronic-phonon coupling and possible superconductivity

Since T_2-, H_1-, and H_3-Nb_2NF_2 are all metal, we further explore the superconductivity of them. The phonon dispersion weighted by the magnitude of EPC λ_{qv}, the in-plane and out-of-plane vibration modes contributed by different elements, the corresponding total and atom-projected phonon DOS, Eliashberg spectral function $a^2F(\omega)$, and cumulative frequency-dependent EPC function $\lambda(\omega)$ are shown in Fig. 4. The properties of T_2-Nb_2NF_2 are included in the SM [40]. For Nb_2NF_2, there are five atoms in each primitive cell, generating 15 phonon branches, with the frequency range

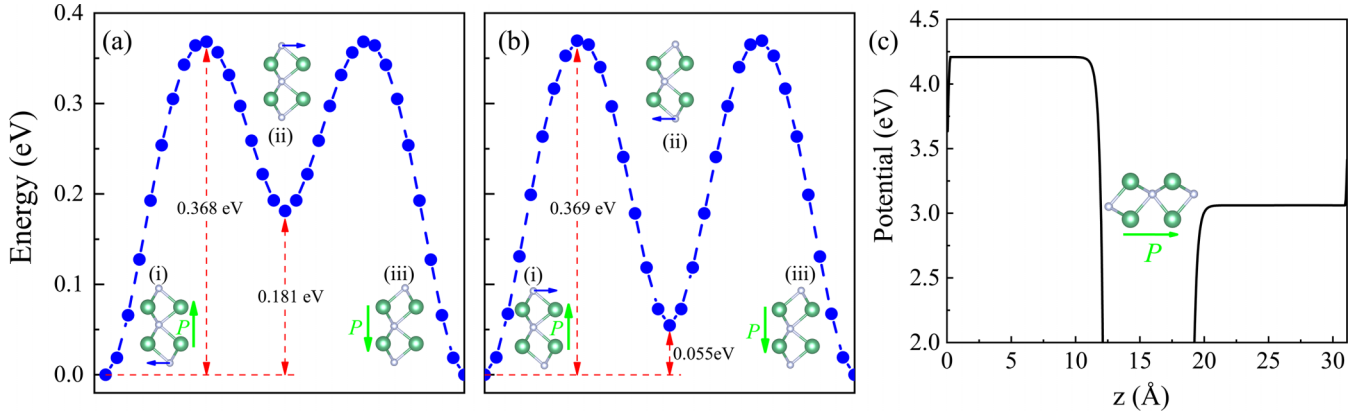

FIG. 3. NEB calculations for polarization direction reversal in H_3-Nb_2NF_2, considering (a) the H_1 and (b) the H_2 nonpolar Nb_2NF_2 as intermediate states. The polarization direction is indicated by the green arrow accompanied by the symbol P. (c) The averaged electrostatic potential of H_3-Nb_2NF_2 in the out-of-plane direction.

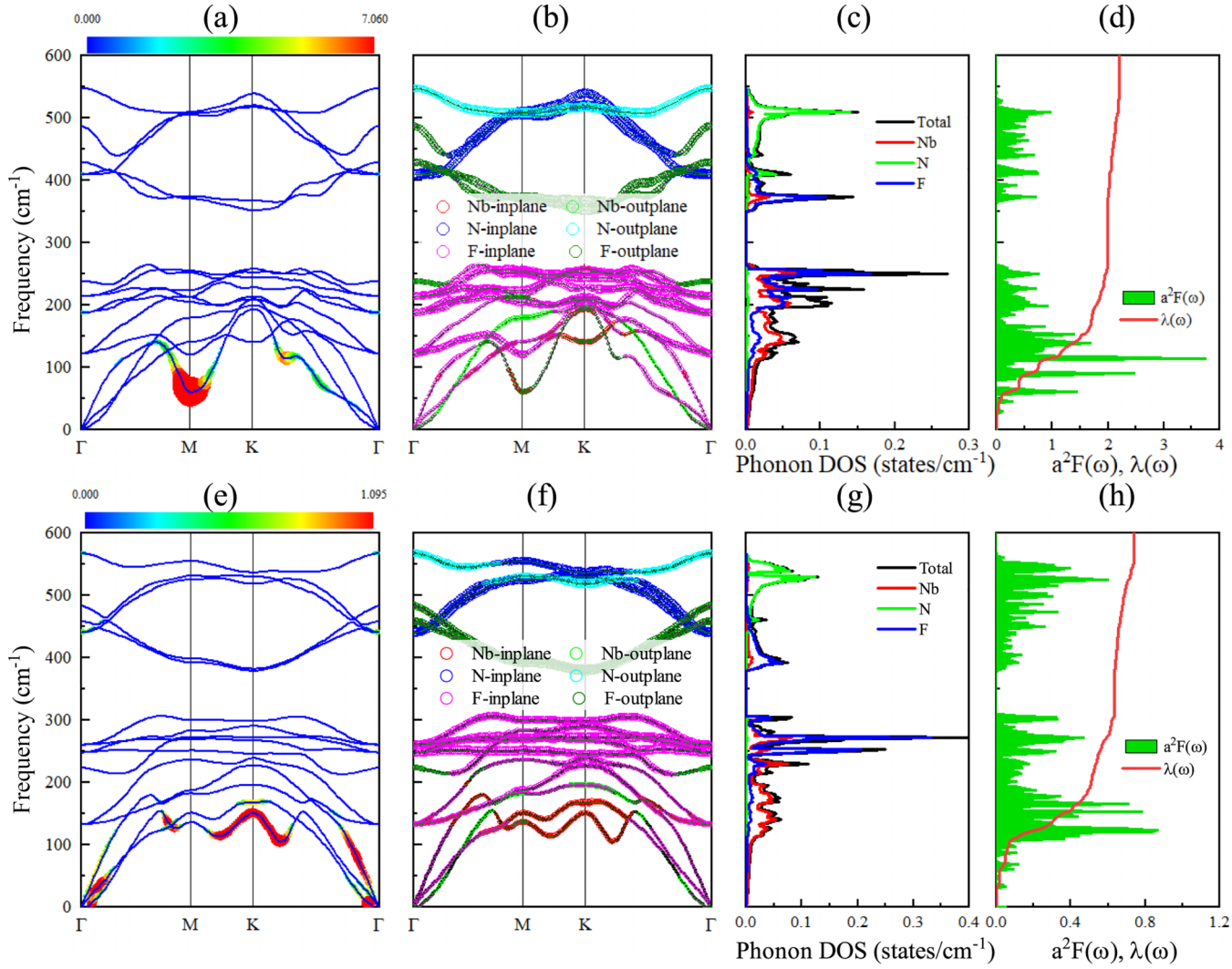

FIG. 4. (a) Phonon dispersion weighted by the magnitude of EPC $\lambda_{q\nu}$ (the magnitude of $\lambda_{q\nu}$ is displayed with different scale in different figures), (b) phonon dispersion weighted by the in-plane and out-plane vibration modes of Nb, N, and F elements, (c) total and atom-projected phonon DOS, (d) Eliashberg spectral function $a^2F(\omega)$ and cumulative frequency-dependent EPC function $\lambda(\omega)$ of H_1-Nb_2NF_2. (e)–(h) are similar to (a)–(d) but for H_3-Nb_2NF_2.

of phonon dispersion up to 600 cm^{-1}. The phonon dispersion weighted by the in-plane and out-plane vibration modes of Nb, N, and F elements of H_1- and H_3-Nb_2NF_2 are shown in Figs. 4(b) and 4(f), where the vibration modes can be clearly divided into two parts. The low-frequency range ($0 < \omega < 320$ cm^{-1}) mainly originates from the vibration modes of Nb and F elements, while the contribution of the N element is relatively small and the high-frequency range ($320 < \omega < 600$ cm^{-1}) is mainly contributed by vibration modes of N and F elements. Combined with the phonon density of state (PhDOS) analysis, it can be seen that the contribution of elements to phonon dispersion is closely related to the atomic mass for both cases, as shown in Figs. 4(c) and 4(g). The contribution of the low-frequency part to phonon dispersion mainly comes from the Nb element with larger atomic mass, the contribution of the midfrequency part comes from the F element, and the contribution of the high-frequency part comes from the N element. Obviously, the positions of the peaks in the Eliashberg spectral function are highly consistent with those of the PhDOS. The Eliashberg spectral function and cumulative frequency-dependent EPC $\lambda(\omega)$ are different for H_1- and H_3-Nb_2NF_2. For H_1-Nb_2NF_2, the frequency-dependent EPC function $\lambda(\omega)$ indicates that the EPC from the low-frequency acoustic branch is stronger that of H_3-Nb_2NF_2, as can also be seen from Figs. 4(a) and 4(e). It results in H_1-Nb_2NF_2 having a higher T_c than H_3-Nb_2NF_2.

Combined with the phonon dispersion weighted by the magnitude of EPC $\lambda_{q\nu}$, the low frequency phonon branches have been softened in H_1-Nb_2NF_2 as compared with the stabilized H_3-Nb_2NF_2. The EPC constant λ and superconductivity critical temperature T_c are calculated through the isotropical momentum-independent Eliashberg function and the McMillan-Allen-Dynes formula [41–43]. According to the McMillian-AllenDynes formula by solving Eqs. (S6)–(S9) in the Supplemental Material [40], the obtained strong coupling f_1 and shape corrections f_2 are considered for the strong EPC cases, i.e., $\lambda > 1.5$. The calculated Eliashberg spectral function $a^2F(\omega)$ and cumulative frequency-dependent EPC function $\lambda(\omega)$ of H_1- and H_3-Nb_2NF_2 are shown in Figs. 4(d) and 4(h), respectively. The λ of H_1-Nb_2NF_2 is 2.91, leading to T_c of 32.1 K, while the λ of H_3-Nb_2NF_2 with the breaking of spatial inversion symmetry is 0.741, and the corresponding T_c is 10.1 K. By analyzing the FS, the total DOS at the Fermi level, phonon dispersion, and EPC strength of Nb_2NF_2 with different symmetry, there are four important aspects related to the enhancement of T_c in H_1-Nb_2NF_2. First, the symmetry will have a significant impact on the charge distribution of the system, especially around the Fermi level. As is well-known, the ferroelectric polarization originates from the breaking spatial inversion symmetry. Then, the DOS at Fermi level and the morphology of the FS are different for the polarized H_3-Nb_2NF_2 and the unpolarized H_1-Nb_2NF_2. Second, as is known, the increasing DOS $N(E_F)$ at the Fermi level will be conducive to the EPC λ. As summarized in Table III, the $N(E_F)$ of H_1-Nb_2NF_2 is enhanced by more than 12.3% from that of H_3-Nb_2NF_2. The increased $N(E_F)$ may further give rise to an enhancement of FS nesting. Third, the FS nesting is beneficial to realize the pairing of electrons for the superconductivity. Fourth, the phonon branches contributed by vibrations of Nb is significant changed because of the different symmetries between H_1-Nb_2NF_2 and H_3-Nb_2NF_2, resulting in an enhancement of λ according to Eq. (4) of the SM [40].

TABLE III. Logarithmic averaged phonon frequency $\omega_{\log}$ (K), electronic DOS at the Fermi level $N(E_F)$ (eV^{-1}), total EPC constant λ, strong-coupling correction factor f_1, shape correction factor f_2, and estimated T_c (K) for 2D Nb_2NF_2.

	$\omega_{\log}$	$N(E_F)$	λ	f_1	f_2	T_c
H_1-Nb_2NF_2	180.81	2.03	2.19	1.15	1.01	32.1
H_3-Nb_2NF_2	245.57	1.81	0.74	1.03	1.00	10.1

The FS nesting χ'', as the imaginary part of the electronic susceptibility at $\omega = 0$, is defined by

$$\lim_{\omega\to 0} \chi''(\mathbf{q},\omega)/\omega = \sum_{\mathbf{k}} \delta(\epsilon_{\mathbf{k}} - \epsilon_F)\delta(\epsilon_{\mathbf{k}+\mathbf{q}} - \epsilon_F), \qquad (1)$$

where ϵ_F is the Fermi energy. To further investigate the EPC of H_1- and H_3-Nb_2NF_2, in Figs. 5(a) and 5(b), the imaginary parts of the bare electronic susceptibility $\chi''(\mathrm{q})$ are shown, which can directly evaluate the FS nesting in the low-frequency limit. As for $\chi''(\mathrm{q})$, it does carry out entire FS nesting into itself near the Γ point, which has no actual physical meaning. For H_1-Nb_2NF_2 another large value of FS nesting appears near the M point, consistent with the large $\lambda_{q\nu}$ around M. To be more clear, in Figs. 4(a) and 4(b), about 60 cm^{-1}, there are softened low-energy phonon branches along the high-symmetry line Γ-M-K-Γ, especially at the M point. The phonons of these positions show large $\lambda_{q\nu}$ in Fig. 4(a). Meanwhile, the imaginary part of the electronic susceptibility, reflecting the nesting effect, shows similar distribution. Therefore, we infer that the nesting effect accounts for the softened phonons in H_1-Nb_2NF_2 and the presence of large EPC $\lambda_{q\nu}$. This phenomenon has also been proposed in transition-metal chalcogenides [46–48]. Thus, we can conclude that strong FS nesting is responsible for the strong EPC in H_1-Nb_2NF_2.

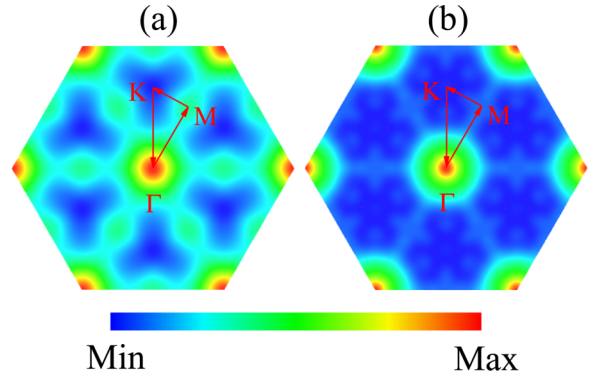

FIG. 5. Imaginary part (Fermi nesting function) $\chi''(\mathrm{q})$ of the electronic susceptibility for (a) H_1- and (b) H_3-Nb_2NF_2. The red, green, and blue regions represent high, middle, and low values of $\chi''(\mathrm{q})$.

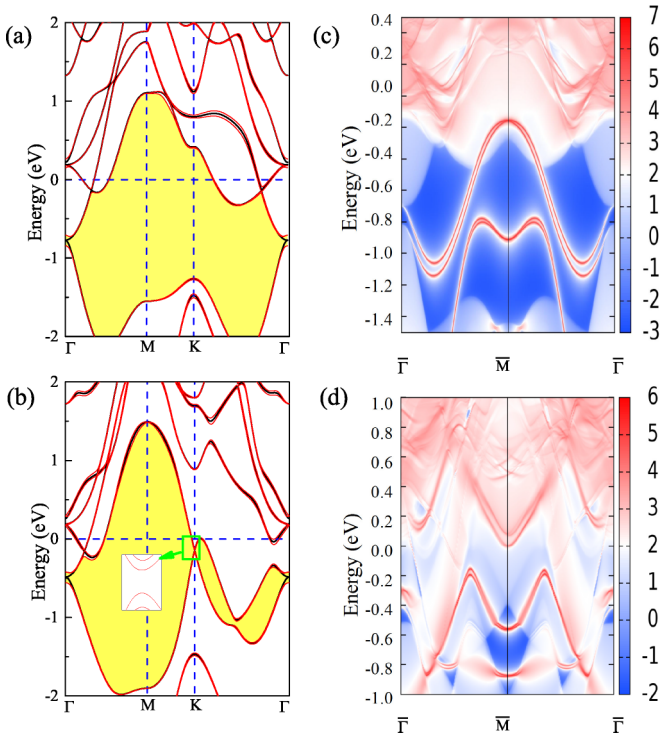

FIG. 6. Band structures for (a) H_1- and (b) H_3-Nb_2NF_2 without (black) and with (red) the SOC. The full gap near the Fermi level for both structures with SOC are decorated by yellow. Edge states of the corresponding semi-infinite slab for (c) H_1- and (d) H_3-Nb_2NF_2. The positive (red end) correspond to higher density of states, and the negative (blue end) denote the bulk band gaps.

D. Topological properties

Then, we investigate the band topology in the 2D Nb_2NF_2. The electronic band structures with and without spin-orbit coupling (SOC) for H_1- and H_3-Nb_2NF_2 along high-symmetry directions are shown in Figs. 6(a) and 6(b), respectively. The bands near the Fermi energy are considered. Both for H_1- and H_3-Nb_2NF_2, the band overlap occurs in the Γ point below Fermi energy as indicated by a green square. When SOC is induced, although there is no global gap, a gap opening occurs at each point in the whole Brillouin zone for both cases. The gap opening with SOC may be accompanied by a topological phase transition. Then, the topological invariant Z_2 is computed based on the Wannier charge-centers (WCC) method [49], which is suitable for the structures with and without spatial inversion symmetry. For H_1- and H_3-Nb_2NF_2, any arbitrary horizontal reference line crosses an odd number of times of WCC, which means a topologically nontrivial state ($Z_2 = 1$). The semi-infinite slab is mainly used to calculate the corresponding edge states when calculating topological properties, so a semi-infinite structural model is constructed to simulate and calculate the edge electronic states of two-dimensional materials. Figures 6(c) and 6(d) show the edge states of H_1- and H_3-Nb_2NF_2 with a semi-infinite slab. The presence of nontrivial topological edge states within the bulk gap can further support the nontrivial band topology. Thus, H_3-Nb_2NF_2 provides a realistic platform for experimental investigations into topological superconductors with tunable ferroelectric properties.

IV. DISCUSSION AND CONCLUSION

Recent investigations have revealed that the external electric field can be a tuning knob for superconductivity in 2D heterojunctions such as bilayer T_d-$MoTe_2$ [7] and twisted graphene [50]. Some of these systems show ferroelectricity properties driven by external electric field. More interestingly, the ferroelectricity of 2D $In_2Se_3/IrTe_2$ heterojunctions cannot only modulate superconductivity but also switch its topological electronic structure between trivial and nontrivial [25]. However, the preparation of high-quality heterojunctions is very difficult due to the lattice matching and interface issues. It is very important to find 2D intrinsic topological superconductor candidates coupled with ferroelectric polarization.

Experimentally, single-layer MXenes-based materials before and after chemical modification have been successfully prepared. For example, the multilayers of $Ti_3C_2T_n$ MXenes (T = Cl, S, NH) was treated with n-butyl lithium (n-BuLi), resulting in Li^+ intercalated sheets with a negative surface charge. Subsequent dispersion in a polar organic solvent such as N-methyl formamide (NMF) resulted in stable colloidal solutions of single-layer flakes [44]. Their work shows that fluorinated MXenes have a more stable structure than other chemically modified MXenes. Therefore, Nb_2NF_2 in this paper may be prepared by this experimental method.

In summary, we have studied the electronic properties and superconductivity of the fluorinated structures of Nb-based MXenes using first-principles calculations and further investigated the ferroelectric properties of the spatial inversion symmetry-breaking structure. The following conclusions can be obtained: (i) Surface fluorination can induce superconductivity in Nb_2N. (ii) Strong Fermi nesting is beneficial for H_1-Nb_2NF_2 to show strong EPC and high-T_c superconductivity. (iii) There is potential ferroelectricity in the asymmetric phase where spatial inversion symmetry is broken. Our research has enriched 2D superconducting materials with nontrivial band topology and ferroelectric properties, and provided a theoretical basis for the preparation of devices switching between superconducting and ferroelectric states with external electric field.

ACKNOWLEDGMENTS

This paper is supported by the National Natural Science Foundation of China (Grants No. 12074213, No. 11574108, and No. 12104253), the Major Basic Program of Natural Science Foundation of Shandong Province (Grant No. ZR2021ZD01), the Natural Science Foundation of Shandong Provincial (Grant No. ZR2023MA082) and the Project of Introduction and Cultivation for Young Innovative Talents in Colleges and Universities of Shandong Province.

[1] F. Xue, J. Zhang, W. Hu, W.-T. Hsu, A. Han, S.-F. Leung, J.-K. Huang, Y. Wan, S. Liu, J. Zhang, J.-H. He, W.-H. Chang, Z. L. Wang, X. Zhang, and L.-J. Li, Multidirection piezoelectricity in mono- and multilayered hexagonal α-In_2Se_3, ACS Nano **12**, 4976 (2018).

[2] L. Kang, P. Jiang, H. Hao, Y. Zhou, X. Zheng, L. Zhang, and Z. Zeng, Giant tunneling electroresistance in two-dimensional ferroelectric tunnel junctions with out-of-plane ferroelectric polarization, Phys. Rev. B **101**, 014105 (2020).

[3] M. Si, A. K. Saha, S. Gao, G. Qiu, J. Qin, Y. Duan, J. Jian, C. Niu, H. Wang, W. Wu, S. K. Gupta, and P. D. Ye, A ferroelectric semiconductor field-effect transistor, Nat. Electron. **2**, 580 (2019).

[4] M. Dai, H. Chen, F. Wang, Y. Hu, S. Wei, J. Zhang, Z. Wang, T. Zhai, and P. Hu, Robust piezo-phototronic effect in multilayer γ-InSe for high-performance self-powered flexible photodetectors, ACS Nano **13**, 7291 (2019).

[5] L. Ju, J. Shang, X. Tang, and L. Kou, Tunable photocatalytic water splitting by the ferroelectric switch in a 2D monolayer, J. Am. Chem. Soc. **142**, 1492 (2020).

[6] S. Yuan, X. Luo, H. L. Chan, C. Xiao, Y. Dai, M. Xie, and J. Hao, Room-temperature ferroelectricity in $MoTe_2$ down to the atomic monolayer limit, Nat. Commun. **10**, 1775 (2019).

[7] A. Jindal, A. Saha, Z. Li, T. Taniguchi, K. Watanabe, J. C. Hone, T. Birol, R. M. Fernandes, C. R. Dean, A. N. Pasupathy, and D. A. Rhodes, Coupled ferroelectricity and superconductivity in bilayer T_d-$MoTe_2$, Nature (London) **613**, 48 (2023).

[8] Z. Fei, W. Zhao, T. A. Palomaki, B. Sun, M. K. Miller, Z. Zhao, J. Yan, X. Xu, and D. H. Cobden, Ferroelectric switching of a two-dimensional metal, Nature (London) **560**, 336 (2018).

[9] W. Luo, K. Xu, and H. Xiang, Two-dimensional hyperferroelectric metals: A different route to ferromagnetic-ferroelectric multiferroics, Phys. Rev. B **96**, 235415 (2017).

[10] J. Lu, G. Chen, W. Luo, J. Íñiguez, L. Bellaiche, and H. Xiang, Ferroelectricity with asymmetric hysteresis in metallic $LiOsO_3$ ultrathin films, Phys. Rev. Lett. **122**, 227601 (2019).

[11] Q. Yang, M. Wu, and J. Li, Origin of two-dimensional vertical ferroelectricity in WTe_2 bilayer and multilayer, J. Phys. Chem. Lett. **9**, 7160 (2018).

[12] X. Liu, Y. Yang, T. Hu, G. Zhao, C. Chen, and W. Ren, Vertical ferroelectric switching by in-plane sliding of two-dimensional bilayer WTe_2, Nanoscale **11**, 18575 (2019).

[13] B. Zhai, B. Li, Y. Wen, F. Wu, and J. He, Prediction of ferroelectric superconductors with reversible superconducting diode effect, Phys. Rev. B **106**, L140505 (2022).

[14] J. Bekaert, C. Sevik, and M. V. Milošević, First-principles exploration of superconductivity in MXenes, Nanoscale **12**, 17354 (2020).

[15] M. Naguib, M. Kurtoglu, V. Presser, J. Lu, J. Niu, M. Heon, L. Hultman, Y. Gogotsi, and M. W. Barsoum, Two-dimensional nanocrystals produced by exfoliation of Ti_3AlC_2, Adv. Mater. **23**, 4248 (2011).

[16] M. Naguib, M. W. Barsoum, and Y. Gogotsi, Ten years of progress in the synthesis and development of MXenes, Adv. Mater. **33**, 2103393 (2021).

[17] R. Ibragimova, P. Erhart, P. Rinke, and H.-P. Komsa, Surface functionalization of 2D mxenes: Trends in distribution, composition, and electronic properties, J. Phys. Chem. Lett. **12**, 2377 (2021).

[18] C. Wang, S. Chen, and L. Song, Tuning 2D mxenes by surface controlling and interlayer engineering: Methods, properties, and synchrotron radiation characterizations, Adv. Funct. Mater. **30**, 2000869 (2020).

[19] N. Jiao, H.-D. Liu, L. Yang, Y.-P. Li, M. Zheng, H.-Y. Lu, and P. Zhang, Hydrogenation-induced high-temperature superconductivity in two-dimensional molybdenum carbide Mo_2C_3, Europhys. Lett. **138**, 46002 (2022).

[20] C. Sevik, J. Bekaert, and M. V. Milošević, Superconductivity in functionalized niobium-carbide mxenes, Nanoscale **15**, 8792 (2023).

[21] J. Bekaert, C. Sevik, and M. V. Milošević, Enhancing superconductivity in MXenes through hydrogenation, Nanoscale **14**, 9918 (2022).

[22] D. Wijethunge, L. Zhang, and A. Du, Prediction of two-dimensional ferroelectric metal MXenes, J. Mater. Chem. C **9**, 11343 (2021).

[23] J.-Y. You, B. Gu, G. Su, and Y. P. Feng, Two-dimensional topological superconductivity candidate in a van der Waals layered material, Phys. Rev. B **103**, 104503 (2021).

[24] Q. Jiang, D. Wang, Z. Liu, Z. Jiang, H. Qian, X. Shen, A. Li, D. Shen, S. Qiao, and M. Ye, Topological surface states in superconducting $CaBi_2$, Phys. Rev. B **104**, 245112 (2021).

[25] J. Chen, W. Qin, P. Cui, and Z. Zhang, Ferroelectric tuning of superconductivity and band topology in a two-dimensional heterobilayer, Phys. Rev. B **108**, L060501 (2023).

[26] P. E. Blöchl, Projector augmented-wave method, Phys. Rev. B **50**, 17953 (1994).

[27] G. Kresse and D. Joubert, From ultrasoft pseudopotentials to the projector augmented-wave method, Phys. Rev. B **59**, 1758 (1999).

[28] G. Kresse and J. Furthmüller, Efficient iterative schemes for ab initio total-energy calculations using a plane-wave basis set, Phys. Rev. B **54**, 11169 (1996).

[29] J. P. Perdew, K. Burke, and M. Ernzerhof, Generalized gradient approximation made simple, Phys. Rev. Lett. **77**, 3865 (1996).

[30] N. A. Spaldin, A beginner's guide to the modern theory of polarization, J. Solid State Chem. **195**, 2 (2012).

[31] W. Yi, G. Tang, X. Chen, B. Yang, and X. Liu, qvasp: A flexible toolkit for VASP users in materials simulations, Comput. Phys. Commun. **257**, 107535 (2020).

[32] V. Wang, N. Xu, J.-C. Liu, G. Tang, and W.-T. Geng, Vaspkit: A user-friendly interface facilitating high-throughput computing and analysis using VASP code, Comput. Phys. Commun. **267**, 108033 (2021).

[33] S. Baroni, S. de Gironcoli, A. Dal Corso, and P. Giannozzi, Phonons and related crystal properties from density-functional perturbation theory, Rev. Mod. Phys. **73**, 515 (2001).

[34] P. Giannozzi, S. Baroni, N. Bonini, M. Calandra, R. Car, C. Cavazzoni, D. Ceresoli, G. L. Chiarotti, M. Cococcioni, I. Dabo, A. D. Corso, S. de Gironcoli, S. Fabris, G. Fratesi, R. Gebauer, U. Gerstmann *et al.*, QUANTUM ESPRESSO: A modular and open-source software project for quantum simulations of materials, J. Phys.: Condens. Matter **21**, 395502 (2009).

[35] H. J. Monkhorst and J. D. Pack, Special points for Brillouin-zone integrations, Phys. Rev. B **13**, 5188 (1976).

[36] M. Kawamura, Fermisurfer: Fermi-surface viewer providing multiple representation schemes, Comput. Phys. Commun. **239**, 197 (2019).

[37] Q. Wu, S. Zhang, H.-F. Song, M. Troyer, and A. A. Soluyanov, WANNIERTOOLS: An open-source software package for novel topological materials, Comput. Phys. Commun. **224**, 405 (2018).

[38] N. Marzari, A. A. Mostofi, J. R. Yates, I. Souza, and D. Vanderbilt, Maximally localized Wannier functions: Theory and applications, Rev. Mod. Phys. **84**, 1419 (2012).

[39] I. Souza, N. Marzari, and D. Vanderbilt, Maximally localized Wannier functions for entangled energy bands, Phys. Rev. B **65**, 035109 (2001).

[40] See Supplemental Material at http://link.aps.org/supplemental/10.1103/PhysRevB.110.094507 for the relevant calculation formulas and calculation details of superconductivity; the phonon spectra of the structures shown in Fig. 1; the electron-phonon coupling properties, the evolution of Wannier charge-centers (wcc), the convergence of band structure with different k-points, and the semi-infinite slab for corresponding structures. The Supplemental Material also contain Refs. [41–43].

[41] W. L. McMillan, Transition temperature of strong-coupled superconductors, Phys. Rev. **167**, 331 (1968).

[42] R. Dynes, Mcmillan's equation and the T_c of superconductors, Solid State Commun. **10**, 615 (1972).

[43] P. B. Allen and R. C. Dynes, Transition temperature of strong-coupled superconductors reanalyzed, Phys. Rev. B **12**, 905 (1975).

[44] V. Kamysbayev, A. S. Filatov, H. Hu, X. Rui, F. Lagunas, D. Wang, R. F. Klie, and D. V. Talapin, Covalent surface modifications and superconductivity of two-dimensional metal carbide mxenes, Science **369**, 979 (2020).

[45] C. Xiao, F. Wang, S. A. Yang, Y. Lu, Y. Feng, and S. Zhang, Elemental ferroelectricity and antiferroelectricity in group-V monolayer, Adv. Funct. Mater. **28**, 1707383 (2018).

[46] J. G. Si, W. J. Lu, H. Y. Wu, H. Y. Lv, X. Liang, Q. J. Li, and Y. P. Sun, Origin of the multiple charge density wave order in 1T-VSe_2, Phys. Rev. B **101**, 235405 (2020).

[47] V. N. Strocov, M. Shi, M. Kobayashi, C. Monney, X. Wang, J. Krempasky, T. Schmitt, L. Patthey, H. Berger, and P. Blaha, Three-dimensional electron realm in VSe_2 by soft-X-ray photoelectron spectroscopy: Origin of charge-density waves, Phys. Rev. Lett. **109**, 086401 (2012).

[48] X. Wang, H. Liu, J. Wu, J. Lin, W. He, H. Wang, X. Shi, K. Suenaga, and L. Xie, 2D materials: Chemical growth of $1T$-TaS_2 monolayer and thin films: Robust charge density wave transitions and high bolometric responsivity, Adv. Mater. **30**, 1870289 (2018).

[49] A. A. Soluyanov and D. Vanderbilt, Computing topological invariants without inversion symmetry, Phys. Rev. B **83**, 235401 (2011).

[50] J. M. Park, Y. Cao, K. Watanabe, T. Taniguchi, and P. Jarillo-Herrero, Tunable strongly coupled superconductivity in magic-angle twisted trilayer graphene, Nature (London) **590**, 249 (2021).